

Communication

Single-Atom Iron Catalyst Based on Functionalized Mesophase Pitch Exhibiting Efficient Oxygen Reduction Reaction Activity

Xianrui Gu ¹, Meng Wang ², Hongpeng Peng ², Qian Peng ¹, Wei Wang ¹, Houpeng Wang ¹, Junjun Shi ¹, Xuetao Qin ², Zhijian Da ^{1,*}, Wenhong Yang ³, Yuchao Wu ^{1,3,*}, Ding Ma ² and Houliang Dai ¹¹ Research Institute of Petroleum Processing, Sinopec, No. 18, Beijing 100083, China² Beijing National Laboratory for Molecular Sciences, College of Chemistry and Molecular Engineering and College of Engineering, and BIC-ESAT, Peking University, Beijing 100871, China³ Petrochemical Research Institute, CNPC, Block E., A42, Beijing 100871, China

* Correspondence: dazhijian@ripp.com (Z.D.); wuyuchao@petrochina.com.cn (Y.W.)

Abstract: Designing highly efficient and low-cost electrocatalysts is of great importance in the fields of energy conversion and storage. We report on the facile synthesis of a single atom (SA) iron catalyst via the pyrolysis of a functionalized mesophase pitch. Monomers of naphthalene and indole underwent polymerization in the presence of iron chloride, which afterwards served as the pore-forming agent and iron source for the resulting catalyst. The SA-Fe@NC catalyst has a well-defined atomic dispersion of iron atoms coordinated by N-ligands in the porous carbon matrix, exhibiting excellent oxygen reduction reaction (ORR) activity ($E_{1/2} = 0.89$ V) that outperforms the commercial Pt/C catalyst ($E_{1/2} = 0.84$ V). Moreover, it shows better long-term stability than the Pt/C catalyst in alkaline media. This facile strategy could be employed in versatile fossil feedstock and develop promising non-platinum group metal ORR catalysts for fuel cell technologies.



Citation: Gu, X.; Wang, M.; Peng, H.; Peng, Q.; Wang, W.; Wang, H.; Shi, J.; Qin, X.; Da, Z.; Yang, W.; et al.

Single-Atom Iron Catalyst Based on Functionalized Mesophase Pitch Exhibiting Efficient Oxygen Reduction Reaction Activity. *Catalysts* **2022**, *12*, 1608. <https://doi.org/10.3390/catal12121608>

Academic Editors: Carlo Santoro and Yongjun Feng

Received: 31 October 2022

Accepted: 2 December 2022

Published: 8 December 2022

Publisher's Note: MDPI stays neutral with regard to jurisdictional claims in published maps and institutional affiliations.



Copyright: © 2022 by the authors. Licensee MDPI, Basel, Switzerland. This article is an open access article distributed under the terms and conditions of the Creative Commons Attribution (CC BY) license (<https://creativecommons.org/licenses/by/4.0/>).

Keywords: functional naphthalene mesophase; single atom catalysis; ORR

1. Introduction

Fuel cells technologies have drawn much attention on account of their applications in the fields of energy conversion and storage [1–3]. The oxygen reduction reaction (ORR) at the cathode is an essential process, which is primarily governed by the precious-group-metal catalysts, such as platinum or its alloy [4]. However, the precious metal-based materials are limited by the high cost and low abundance in nature, impeding the commercialization of the fuel cells. Therefore, efforts have been devoted to developing non-precious metal catalysts [5,6]. Metal–nitrogen–carbon (M–N–C, M = Fe, Co) materials are promising candidates for electrochemical reactions in place of the Pt-based catalysts [7–17]. For Fe–N–C materials, nitrogen-coordinated iron atoms (Fe–N_x species) dispersed in the porous carbon matrix are considered as the active sites, exhibiting high ORR activities [18–21]. The Fe–N–C catalysts are generally fabricated by pyrolysing precursors containing Fe, N and C [22,23], for example, metal complexes with N_x-macrocycles [24,25], nitrogen-containing polymers [3,26–28] and biomass [29]. However, these synthesis methods usually require iron salts mixing, which is time consuming and likely induces inhomogeneity to the catalysts, consequently influencing the ORR activity. Moreover, metal–organic frameworks (MOFs) [30–33] and template-assisted nanomaterials have been investigated, which could efficiently enhance the dispersity of iron atoms in the pyrolyzed matrix [20,34,35], yet these suffer from high cost and low yield; thus, they could be hardly applied to large-scale manufacturing.

To overcome the problems as mentioned above, we developed an efficient and versatile method to fabricate a single-atom iron catalyst on N-doped carbon networks (SA-Fe@NC). The precursor of the catalyst comes from a mesophase pitch, which is considered as an excellent intermediate for advanced carbon materials such as carbon foam [36], carbon fiber [37],

needle coke and C/C composites [38,39]. This pitch material is commonly obtained from the petroleum by-products with abundant aromatic fractions, for example, fluid catalytic cracking decant oil [40]. Minato et al. reported the polymerization of naphthalene into carbonaceous mesophase using a Lewis acid AlCl_3 as the catalyst [41]. This was further developed with more efficient catalysts and more diversified aromatic raw materials [40,42]. In this work, we synthesized the nitrogen-enriched naphthalene pitch (NP) via the copolymerization of naphthalene and indole, which are catalyzed by the Lewis acid iron chloride. N-containing molecules could be easily oligomerized via Friedel–Crafts reaction and dispersed into the carbon matrix, introducing more functionalities to the carbonaceous precursors. Meanwhile, the iron chloride also serves as the pore-forming agent and the source of active sites in the subsequent pyrolysis process. The as-synthesized catalyst exhibits efficient ORR activity with $E_{1/2}$ (half-wave potential) of 0.89 V in 0.1 M KOH, which is 50 mV more positive than that of the commercial Pt/C ($E_{1/2}$ of 0.84 V). Moreover, it also shows better methanol tolerance and excellent stability compared to the commercial Pt/C catalyst, displaying no obvious current change in the presence of 1.0 M MeOH and little drop in $E_{1/2}$ after 5000 potential cycles. The high ORR activity is attributed to the atomically dispersed Fe–N_x sites which are confirmed by X-ray photoelectron spectroscopy (XPS), high-angle annular dark-field scanning transmission electron microscope (HAADF-STEM) and extended X-ray absorption fine structure (EXAFS) results. Considering that the naturally acquired crude oil contains an abundance of heteroaromatics such as aniline, indole, pyridine and pyrrole [43], the present synthesis of SA-Fe@NC provides a novel means toward active and low-cost ORR catalysts and offers a new route for utilizing the petroleum resources.

2. Results and Discussion

The fabrication process of the SA-Fe@NC catalyst is shown in Figure 1. Monomers of naphthalene and indole oligomerized in the presence of FeCl_3 , forming an NP carbonaceous precursor. This process was performed in a mild solvent-free condition and can be easily enlarged into large scale. The precursor was sampled and analyzed via Fourier transform ion cyclotron resonance mass spectrometry (FT-ICR MS). Under the atmospheric pressure photo ionization (APPI) mode, naphthalene oligomers and dehydrogenized co-polymers of indole–naphthalene can be observed between 800 and 1200 Da (Figure S1, Supplementary Material). Switching to the ESI^- mode, more co-polymers of indole–naphthalene are detected as they are more likely to be ionized by the ESI^- source. Patterned peaks are observed between 900 and 1200 Da on account of the length difference in co-polymers. Peaks (labeled in red) with m/z of 903.3359, 1043.3635 and 1158.4072 Da confirm the polymerization between naphthalene and indole (Figure 1). After pyrolyzing the precursor at 800 °C under N_2 atmosphere, followed by acid leaching, the catalyst SA-Fe@NC₈₀₀ was obtained. Brunauer–Emmet–Teller (BET) measurements were carried out and are shown in Figure 2a. The surface area and pore volume of the SA-Fe@NC₈₀₀ are 289 m^2/g and 0.22 cm^3/g , respectively. These values are much higher than the control sample (7.29 m^2/g and 0.04 cm^3/g) prepared with AlCl_3 as the polymerizing agent in replacement of FeCl_3 (Figure S2, Supplementary Material), suggesting the pore-forming ability of the latter during the pyrolysis process [44]. The pore size distribution curve (Figure 2a inset) also shows the abundance of mesopores in the catalyst. The graphitization degree of the catalysts was confirmed by Raman spectroscopy. In Figure 2b, two peaks are located at ca. 1374 cm^{-1} and 1594 cm^{-1} for the SA-Fe@NC₈₀₀, representing the D-band and G-band of graphite, respectively.

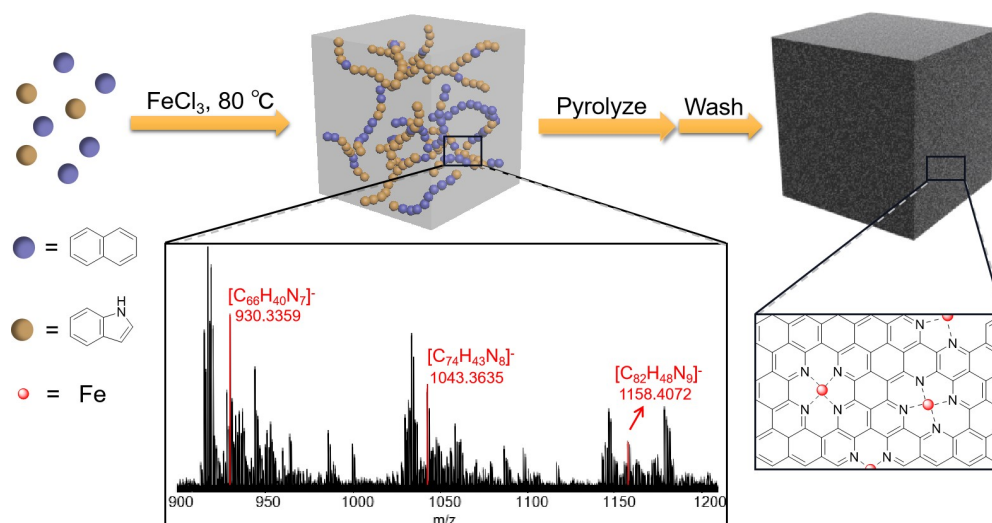


Figure 1. Schematic illustration of the synthesis procedure of the SA-Fe@NC.

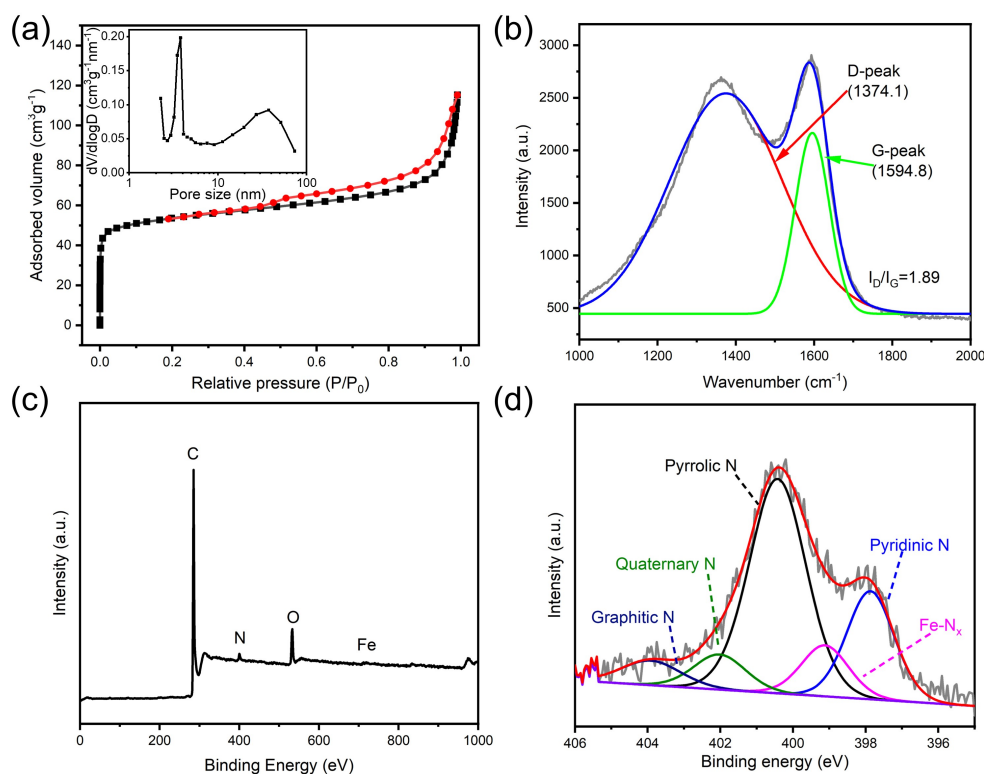


Figure 2. (a) N₂ adsorption–desorption isotherm (inset: pore size distribution), (b) Raman spectrum, (c) XPS survey scan spectrum and (d) the corresponding high-resolution N 1s spectrum of the SA-Fe@NC₈₀₀.

The corresponding I_D/I_G values are employed to analyze the degree of graphitic nature of the prepared samples. As the pyrolysis temperature of the SA-Fe@NC increased from 800 to 950 °C, the I_D/I_G ratio dropped from 1.89 to 1.34, indicating the formation of more ordered graphitic structures. However, when the pyrolysis temperature further increased to 1100 °C, the I_D/I_G ratio augmented to 1.46, which was likely on account of the formation of defects at higher temperature (Figures S3 and S4, Supplementary Material). XPS spectrum reveals the elemental composition of the SA-Fe@NC₈₀₀ catalyst. From the survey scan of the SA-Fe@NC₈₀₀ (Figure 2c), the C, N, O and Fe elements are determined to be 90.2%, 3.72%, 5.98%, and 0.43%, respectively. The nitrogen content decreased with the

augment of pyrolysis temperature from 800 to 1100 °C (Figure S5 and Table S1, Supporting Information). When the feeding ratio between indole and naphthalene was tuned down to 1:5 during the preparation of precursor, the nitrogen content of the catalyst (SA-Fe@NC₈₀₀₋₁) dropped correspondingly. Yet when the indole was solely polymerized, the pyrolyzed catalyst (SA-Fe@NC₈₀₀₋₂) showed a significant decrease in the nitrogen content (Table S1, Supporting Information), possibly owing to the lower decomposition temperature of indole oligomers [45]. The high-resolution N 1s spectra of the SA-Fe@NCs at different temperature are further deconvoluted into five component peaks at 397.9, 399.1, 400.4, 402.1 and 403.9 eV (Figure 2d, Figures S6 and S7 in the Supplementary Material), corresponding to pyridinic N, Fe-N_x, pyrrolic N, graphitic N and quaternary N, respectively, and the results are summarized in Table S2, Supporting Information [46]. Among them, pyridinic N and pyrrolic N can serve as metal-coordination sites on account of their lone-pair electrons. Higher ratios of both kinds of N likely promote the gain of resulting Fe-N_x, which are generally considered as beneficial to the ORR [27]. The SA-Fe@NC₈₀₀ follows this trend, revealing higher proportions of pyridinic N (0.83%), pyrrolic N (1.96%) and Fe-N_x (0.39%) than the rest SA-Fe@NC catalysts.

The morphology of the SA-Fe@NC₈₀₀ was investigated by scanning electron microscopy (SEM) and transmission electron microscopy (TEM). Multilayers of the catalysts are observed, stacking to form structures with hierarchical pores (Figure 3a and Figure S8 in the Supplementary Material). The mapping images reveal that C, N, and Fe elements are uniformly distributed over the entire structure, as shown in Figure 3b, which is consistent with the XPS results in Figure 2c,d. At higher magnification, Figure 3c depicts the annular bright field (ABF) STEM image. Flake-like graphitic carbon structures are clearly observed, with no existing Fe particles. The HAADF-STEM images at the same region (Figure 3d,e) demonstrate highly dispersed Fe single atoms, which are identified by the isolated bright dots marked with yellow cycles. To further confirm the existence of atomically dispersed iron atoms, the X-ray absorption near-edge structure (XANES) and EXAFS measurements were performed. The XANES spectra (Figure 4a) show that the absorption edge of the SA-Fe@NC₈₀₀ lies in between the FeO and Fe₂O₃, indicating its Fe atom valency fluctuates between Fe⁰ and Fe³⁺. In addition, the shoulder peak of the SA-Fe@NC₈₀₀ at ca. 7114 eV discloses the fingerprint of the square-planar Fe-X₄ moiety (D_{4h} symmetry), which suggests the existence of the Fe-N₄ structure [47,48]. Meanwhile, the EXAFS spectra of K-edge show a peak at around 1.6 Å, and no apparent Fe-Fe coordination peak or other high shell peaks are observed (Figure 4b), indicating the formation of atomically dispersed Fe-N/O sites [18,49]. The coordination number of Fe within the Fe-N/O sites was calculated as 5 (Table S3, Supporting Information), suggesting a porphyrin planar structure of Fe-N₄ with an O₂ molecule absorbed vertically [33].

As an atomically dispersed Fe catalyst, the unique features of the SA-Fe@NCs imply themselves being ORR active. The ORR activities of the catalysts were firstly evaluated by cyclic voltammetry (CV) measurements in N₂- and O₂-saturated 0.1 M KOH solutions. In contrast to the featureless CV curves across the entire potential range in the N₂ solution, obvious cathodic peaks appear in the CV curves of all the catalysts in the O₂ solution owing to the oxygen reduction (Figure 5a and Figure S9 in the Supplementary Material). The SA-Fe@NC₈₀₀ catalyst displays a more positive cathodic peak potential (0.85 V vs. RHE (Reversible Hydrogen Electrode), the same hereafter) than the commercial Pt/C catalyst (0.82 V) and other SA-Fe@NC catalysts pyrolyzed at higher temperatures, implying a higher ORR activity. Figure 5b shows the polarization curve of the catalysts in the O₂-saturated 0.1 M KOH electrolyte at a rotating speed of 1600 rpm. The SA-Fe@NC₈₀₀ shows the highest half-wave potential (E_{1/2}) of 0.89 V and the onset potential (E_{onset}) of 1.06 V, which is much higher ORR activity than the SA-Fe@NC catalysts pyrolyzed at higher temperatures and the SA-Fe@NC catalysts with different compositions (Figure S10, Supplementary Material). In addition, the optimized E_{1/2} and E_{onset} are higher than that of the commercial Pt/C catalyst (E_{1/2} = 0.84 V, E_{onset} = 0.97 V).

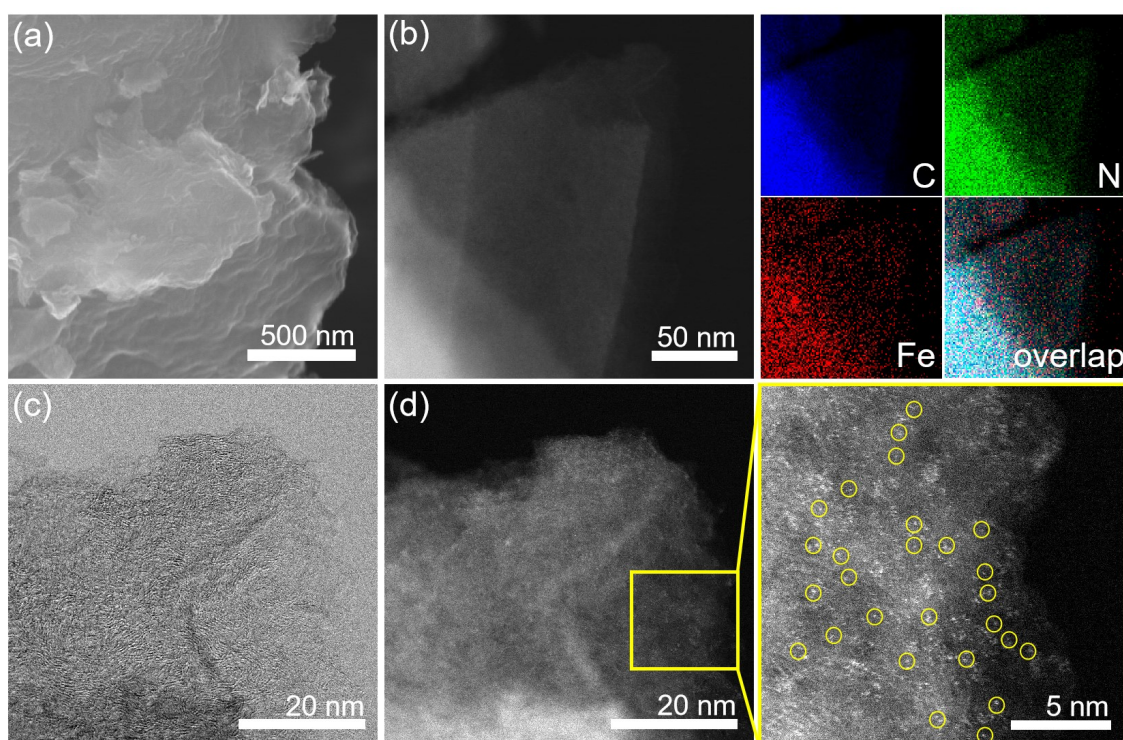


Figure 3. Microscopic characterization of the SA-Fe@NC₈₀₀. (a) SEM image, (b) HAADF-STEM image and elemental mapping, C (blue), N (green) Fe (red) and overlay. (c) ABF image, (d) HAADF-STEM image and the enlarged view.

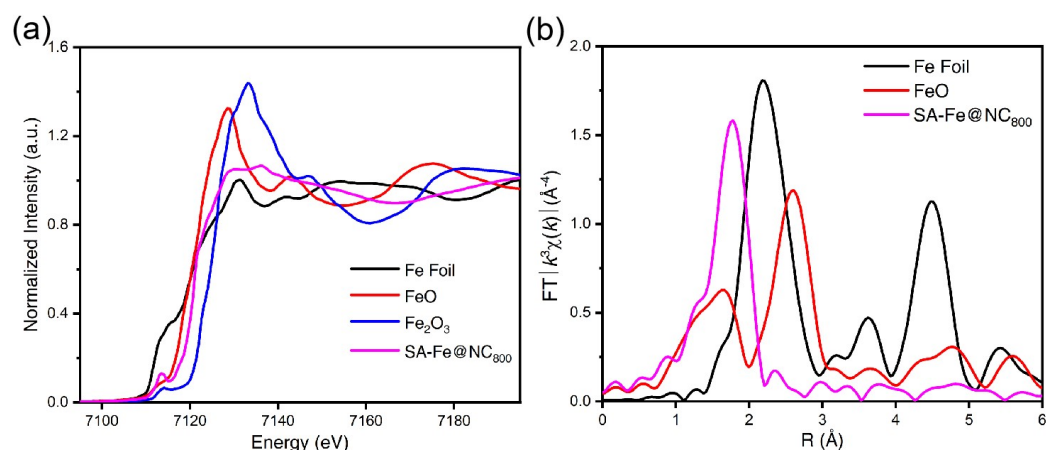


Figure 4. (a) XANES spectra at the Fe K-edge of the SA-Fe@NC₈₀₀, FeO, Fe₂O₃ and Fe foil. (b) Fourier transform (FT) at the Fe K-edge of the SA-Fe@NC₈₀₀, FeO and Fe foil.

As shown in Figure 5c, the RDE polarization curves of SA-Fe@NC₈₀₀ at various rotating speeds are studied, and the corresponding Koutecky–Levich (K-L) plots at different applied potentials display linear relationships with the first-order reaction kinetics. The transfer electron number calculated by the K-L plots is 3.8 from a potential range of 0.5–0.7 V, indicating a dominant four-electron transfer pathway.

The ORR kinetics of the catalyst was further analyzed by Tafel plots. The Tafel slope of the SA-Fe@NC₈₀₀ (86 mV dec^{−1}) is smaller than that of the commercial Pt/C, suggesting a faster current increasing rate in the former (Figure 5d). Furthermore, the methanol tolerance of the SA-Fe@NC₈₀₀ was evaluated by the chronoamperometric measurements in the O₂-saturated 0.1 M KOH electrolyte at 0.8 V with a rotation rate of 1600 rpm. A significant change in the current density is observed for the Pt/C after the addition of methanol to the electrolyte. While the catalyst SA-Fe@NC₈₀₀ shows little change in the current density

against the methanol injection across the entire observation time, indicating remarkable tolerance to methanol crossover (Figure 5e). In addition, the durability of SA-Fe@NC₈₀₀ was evaluated by cycling the catalyst between 0.6 and 1.0 V at a scan rate of 50 mV s⁻¹ in O₂-saturated 0.1 M KOH, as shown in Figure 5f. After 5000 continuous cycles, there is very little decay in E_{1/2} (ca. 3 mV), demonstrating the outstanding stability of the SA-Fe@NC₈₀₀. In contrast, the commercial Pt/C is subjected to a drop of nearly 40 mV in E_{1/2} (Figure S11, Supplementary Material). Meanwhile, in the long-term chronoamperometric measurements (0.8 V), the current density retains at 93.6% over 12,000 s continuous working for SA-Fe@NC₈₀₀, while the commercial Pt/C shows only 67.5% retention of the current density under the same condition (Figure S12, Supplementary Material).

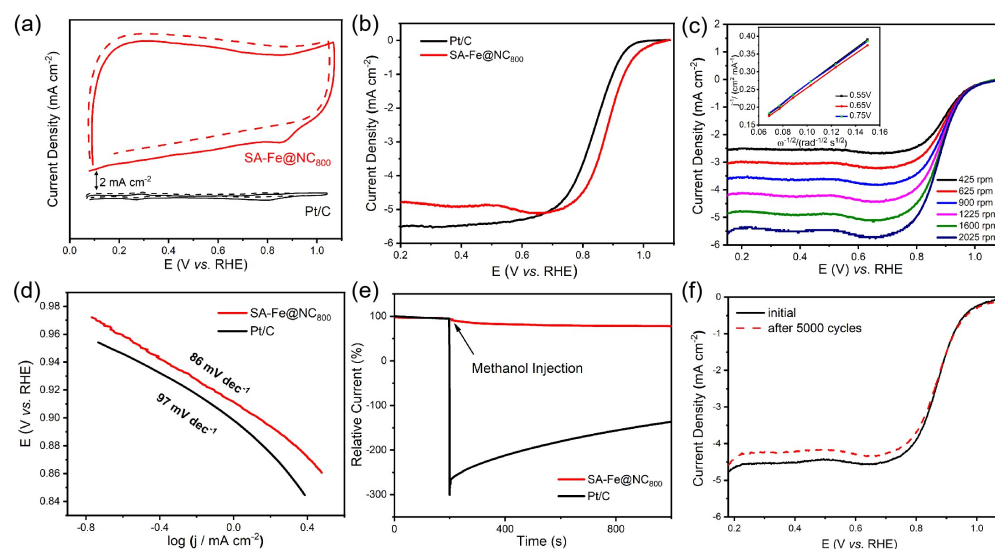


Figure 5. (a) CV curves of the SA-Fe@NC₈₀₀ and the commercial Pt/C catalysts in the O₂-saturated (solid line) and N₂-saturated (dashed line) 0.1 M KOH solutions at a sweep rate of 50 mV s⁻¹. (b) LSV curves of the catalysts in the O₂-saturated 0.1 M KOH electrolyte at 10 mV s⁻¹ with a rotation rate of 1600 rpm. (c) LSV curves of the SA-Fe@NC₈₀₀ in the O₂-saturated 0.1 M KOH solution at 50 mV s⁻¹ with different rotation rates (inset shows the corresponding Koutechy–Levich plots). (d) Tafel plots of the SA-Fe@NC₈₀₀ in 0.1 M KOH. (e) Methanol crossover effect test of the SA-Fe@NC₈₀₀ and Pt/C at 0.8 V. 3 mL of methanol was injected into the O₂-saturated 0.1 M KOH solution (90 mL) at 200 s. (f) LSV curves of SA-Fe@NC₈₀₀ before and after 5000 CV cycles between 0.6 and 1.0 V.

3. Materials and Methods

All chemicals were used as received without further purification. Hydrochloric acid (HCl, >36%), naphthalene (99%), indole (99%), and anhydrous ferric chloride (FeCl₃) were purchased from Sinopharm Chemical Ltd., Beijing, China, Potassium hydroxide (KOH, 99.99%) was obtained from Aladdin, Beijing, China. Commercial Pt/C (20 wt % metal) and Nafion solution (5 wt %) were supplied by Alfa Aesar. All the water in the experiments was ultrapure water (>18.2 MΩ cm).

TEM images were performed on a Technai F20 transmission electron microscope. The high-resolution TEM, HAADF-STEM images and elemental mapping were recorded on a JEOL-2100F FETEM with electron acceleration energy of 200 kV. Photoemission spectroscopy experiments (XPS) were performed at the Photoemission Endstation at the BL10B beamline. XAFS spectra at the Fe K-edge were measured at the beamline 1W1B station of the Beijing Synchrotron Radiation Facility (BSRF), China. The Fe K-edge XAFS data were recorded in a fluorescence mode. Fe foil, Fe₂O₃ were used as references. All spectra were collected in ambient conditions. The acquired EXAFS data were processed according to the standard procedures using the ATHENA module implemented in the IFEFFIT software packages (version 0.9.25, Chicago, IL, USA). The k³-weighted EXAFS spectra were obtained by subtracting the post-edge background from the overall absorption

and then normalizing with respect to the edge-jump step. Subsequently, the k^3 -weighted $x(k)$ data of Fe K-edge were Fourier transformed to real (R) space using a hanning windows ($dk = 1.0 \text{ \AA}^{-1}$) to separate the EXAFS contributions from different coordination shells.

3.1. Negative ESI FT-ICR MS Characterization

The co-polymer of naphthalene and indole was dissolved in toluene to yield a stock solution of 10 mg/mL. The stock solution was then diluted to 0.02 mg/mL in toluene/methanol ($v:v = 1:1$). Ammonia hydroxide (28%) was added to the diluted solution, and the final base concentration was 2.5% ($v:v$). The prepared sample flowed through a fused-silica capillary at a rate of 120 $\mu\text{L/h}$ by a syringe pump. Analyses were conducted on a 15 T Bruker Solarix XR FT-ICR MS. The ionization source was negative mode electrospray ionization (ESI). Nitrogen (99.999%) served as the drying gas and nebulizing gas. The drying gas flow rate was 4.0 L/min at the temperature of 200 °C. The nebulizing gas flow rate was 1.0 L/min. The skimmer voltage was 15 V. The m/z range was from 50 to 3000 Da. The RF amplitudes of the collision hexapole were 800 Vpp. The time-of-flight was 1.0 ms. The data size was 8 M and time-domain data sets were 128 scans.

3.2. Positive APPI FT-ICR MS Characterization

The co-polymer of naphthalene and indole was dissolved in toluene to yield a stock solution of 10 mg/mL. The stock solution was then diluted to 0.02 mg/mL in toluene. The prepared sample flowed through a fused-silica capillary at a rate of 360 $\mu\text{L/h}$ by a syringe pump. Analyses were conducted on a 15 T Bruker Solarix XR FT-ICR MS. Positive mode atmospheric pressure photoionization (APPI) was used as the ionization source and the light source was a Kr lamp. Nitrogen (99.999%) served as the drying gas and nebulizing gas. The temperature of the drying gas was 200 °C and the flow rate was 2.0 L/min. The nebulizing gas flow rate was 1.0 L/min, and the temperature of vaporizer was 400 °C. The skimmer voltage was 15 V. The m/z range was from 50 to 3000 Da. The RF amplitudes of the collision hexapole were 1000 Vpp. The time-of-flight was 1.8 ms. The data size was 8 M and time-domain data sets were 128 scans.

3.3. Electrochemical Measurement

All catalysts were prepared by mixing 6 mg of the catalyst in 1 mL of solution containing 300 μL of ethanol, 660 μL of H_2O and 40 μL of 5% Nafion solution, which was followed by ultrasonication for 1 h to form homogeneous catalyst inks. Commercial 20 wt % Pt/C was prepared as a 5 mg/mL solution. To achieve a desirable catalyst loading, a certain volume of the catalyst ink was carefully dropped to a well-polished glassy carbon (GC) rotating disk electrode (RDE). In order to prevent the contamination of catalysts, the GC electrode was polished using 0.05 μm alumina slurry, rinsed with deionized water, and then ultrasonicated in water for 30 s (3 times) and washed with distilled water until the appearance of a mirror-like surface on the GC electrode. Finally, the nonprecious catalyst loading was $0.510 \text{ mg}\cdot\text{cm}^{-2}$, and the loading of Pt/C was $0.127 \text{ mg}\cdot\text{cm}^{-2}$.

Electrochemical measurements were carried out in a three-electrode system on a Pine biopotentiostat electrochemical workstation (Pine Instrument Co., Durham, NC, USA) in 0.1 M KOH electrolyte. A rotating disk electrode (RDE) with a GC disk of 5 mm in diameter was used as the substrate for the working electrode, and a carbon rod was used as the counter electrode. The potential was recorded by a Ag/AgCl (saturated KCl solution) electrode as the reference electrode. Oxygen flow was used through the electrolyte in the cell for 30 min to saturate it with O_2 before a measurement, and all electrochemical experiments were conducted in 0.1 M KOH at room temperature. The cyclic voltammetry (CV), linear sweep voltammetry (LSV), accelerated durability and chronoamperometric tests were carried out to measure the electrochemical performance of the catalyst. The

measured potentials vs. Ag/AgCl were converted to a reversible hydrogen electrode (RHE) scale according to the Nernst equation:

$$E_{RHE}(V) = E_{Ag/AgCl} + E_{Ag/AgCl}^0 + 0.059pH$$

where $E_{Ag/AgCl}^0 = 0.1976$ V at 25 °C, $E_{Ag/AgCl}$ is the experimentally measured potential against the Ag/AgCl reference electrode, and ERHE is the converted potential vs. RHE.

CV experiments measure the electrochemical ability by recording the current variation of oxidation reduction reaction within a certain potential range. The electrolyte was saturated with oxygen before each experiment, the potential zone of CV tests were between 0 and 1.2 V (vs. RHE), the scan rate was $50 \text{ mV}\cdot\text{s}^{-1}$, and at least 10 cycles were performed before collecting the data. During the experiment, a flow of O_2 was maintained over the electrolyte to ensure the O_2 saturation. In addition, tests were also performed in N_2 saturated electrolyte with a scan rate of $50 \text{ mV}\cdot\text{s}^{-1}$ to measure the background current. Linear sweep voltammetry (LSV) tests were measured at various rotating speed from 400 to 2500 rpm with a scan rate of $10 \text{ mV}\cdot\text{s}^{-1}$ in O_2 -saturated electrolyte. An accelerated durability test (ADT) was carried out by cycling the catalysts between 0.6 and 1.05 V (vs. RHE) at a scan rate of $50 \text{ mV}\cdot\text{s}^{-1}$. To evaluate the stability of the catalyst, the LSV curve of the catalyst was measured after 5000 cycles and compared with its initial LSV curve. A chronoamperometric test (CA) was performed to test the methanol tolerance and the electrochemical durability of the catalysts. At a constant potential (0.8 V vs. RHE), the decline rate of the current was recorded after 12,000 s. For the methanol tolerance, 3 mL of methanol was injected into the electrolyte at 200 s.

The electron transfer number (n) and kinetic current density (j_k) were examined by the Koutecky–Levich equation:

$$\frac{1}{j} = \frac{1}{j_l} + \frac{1}{j_k} = \frac{1}{B\omega^{1/2}} + \frac{1}{j_k}$$

$$B = 0.62nFC_0D_0^{2/3}V^{-1/6}$$

where j is the measured current density, j_k and j_l are the kinetic and limiting current densities, ω is the angular velocity of the disk, n is the electron transfer number, F is the Faraday constant ($96485 \text{ C}\cdot\text{mol}^{-1}$), C_0 is the bulk concentration of O_2 ($1.2 \times 10^{-6} \text{ mol}\cdot\text{cm}^{-3}$), D_0 is the diffusion coefficient of O_2 ($1.9 \times 10^{-5} \text{ cm}^2\cdot\text{s}^{-1}$), and V is the kinematic viscosity of the electrolyte ($0.01 \text{ cm}^2\cdot\text{s}^{-1}$).

3.4. Preparation of SA-Fe@NC

Typically, 25.6 g of naphthalene and 11.7 g of indole were ground and placed in a 200 mL three-necked round-bottom flask, which was followed by the addition of powdered FeCl_3 (anhydrous). The mixture was stirred under nitrogen atmosphere at 85 °C for 4 h. Then, at room temperature, the solidified black product was transferred into a ceramic boat and placed in a tube furnace. Samples were heated to 800 °C, 950 °C and 1100 °C respectively with a heating rate of $5 \text{ }^\circ\text{C}\cdot\text{min}^{-1}$ and kept at 800 °C, 950 °C and 1100 °C, respectively, for 3 h under the flowing argon gas ($150 \text{ mL}\cdot\text{min}^{-1}$) and then naturally cooled to room temperature. The obtained black powder were leached by 0.4 M HCl at 60 °C for 12 h, and the finally obtained black powder were named as SA-Fe@NC₈₀₀, SA-Fe@NC₉₅₀ and SA-Fe@NC₁₁₀₀, respectively. The control sample was prepared at the same condition with AlCl_3 as catalyst and pyrolyzed at 800 °C. The sample SA-Fe@NC₈₀₀₋₁ was prepared from the precursor with 25.6 g of naphthalene and 4.68 g of indole in the presence of catalyst FeCl_3 , which was followed by the pyrolysis at 800 °C and acid leaching. The sample SA-Fe@NC₈₀₀₋₂ was prepared from the precursor with only 11.7 g indole in the presence of catalyst FeCl_3 , which was followed by the pyrolysis at 800 °C and acid leaching.

4. Conclusions

An efficient and versatile strategy was developed for the fabrication of atomically dispersed iron catalyst on carbonaceous materials. Lewis acid FeCl_3 plays multiple roles, including polymerization catalyst (the Lewis acid), pore-forming agent and iron source. With the assistance of comprehensive characterization techniques including XPS, HRTEM and XAFS, the atomically dispersed Fe active sites with an optimized coordination environment in the hierarchical porous carbon matrix are confirmed. The obtained SA-Fe@NC outperforms the commercial Pt/C catalyst in terms of ORR activity, tolerance of methanol crossover and long-term stability. This strategy could be employed in building Fe/N-modified carbon materials from fossil feedstock for potential large-scale commercial applications.

Supplementary Materials: The following supporting information can be downloaded at: <https://www.mdpi.com/article/10.3390/catal12121608/s1>, Figure S1: FT-ICR-MS results under the atmospheric pressure photo ionization (APPI) mode, (a) peaks show the presence of the naphthalene polymers and (b) peaks show the presence of the dehydrogenized co-polymers of indole-naphthalene; Figure S2: BET results for the control sample using AlCl_3 as polymerization catalyst; Figure S3: Raman of SA-Fe@NC₉₅₀; Figure S4: Raman of SA-Fe@NC₁₁₀₀; Figure S5: XPS survey scan spectra of SA-Fe@NC₉₅₀, SA-Fe@NC₁₁₀₀, SA-Fe@NC₈₀₀₋₁ and SA-Fe@NC₈₀₀₋₂; Figure S6: XPS of SA-Fe@NC₉₅₀; Figure S7: XPS of SA-Fe@NC₁₁₀₀; Figure S8: SEM of SA-Fe@NC₈₀₀ showing structures with hierarchical pores; Figure S9: (a) CV curves of SA-Fe@NC₈₀₀, SA-Fe@NC₉₅₀, SA-Fe@NC₁₁₀₀ and Pt/C catalysts in O_2 -saturated (solid line) and N_2 -saturated (dashed line) in 0.1 M KOH solutions at a sweep rate of 50 mV s^{-1} . (b) LSV curves of above catalysts in O_2 -saturated 0.1 M KOH electrolyte at 10 mV s^{-1} with a rotation rate of 1600 rpm; Figure S10: (a) CV curves of SA-Fe@NC₈₀₀₋₁, SA-Fe@NC₈₀₀₋₂ and Pt/C catalysts in O_2 -saturated (solid line) and N_2 -saturated (dashed line) in 0.1 M KOH solutions at a sweep rate of 50 mV s^{-1} . (b) LSV curves of above catalysts in O_2 -saturated 0.1 M KOH electrolyte at 10 mV s^{-1} with a rotation rate of 1600 rpm; Figure S11: LSV curves for Pt/C before and after 5000 CV cycles between 0.6 and 1.0 V; Figure S12: Stability test of the SA-Fe@NC₈₀₀ and the commercial Pt/C in the O_2 -saturated 0.1 M KOH solution at 0.8 V under a rotation rate of 1600 rpm; Table S1: Elemental compositions of SA-Fe@NC catalysts determined by XPS.; Table S2: N contents of SA-Fe@NC catalysts pyrolyzed at different temperatures obtained from XPS N 1s spectra; Table S3: Structural parameters extracted from the Fe K-edge EXAFS fitting.

Author Contributions: Formal analysis, M.W., H.P., Q.P., X.G., W.W., H.W., J.S., X.Q.; writing—original draft preparation, Y.W.; writing—review and editing, Y.W.; Validation, W.Y.; supervision, D.M., Z.D., H.D.; project administration, Z.D., H.D. All authors have read and agreed to the published version of the manuscript.

Funding: This work received financial support from the Natural Science Foundation of China (22005007, 21725301, 21932002, 21821004), and the National Key R&D Program of China (2019YFB1505000, 2017YFB0602200).

Data Availability Statement: Not applicable.

Conflicts of Interest: The authors declare no conflict of interest.

References

1. Debe, M.K. Electrocatalyst approaches and challenges for automotive fuel cells. *Nature* **2012**, *486*, 43–51. [[CrossRef](#)] [[PubMed](#)]
2. Ellingsen, L.A.W.; Hung, C.R.; Majeau-Bettez, G.; Singh, B.; Chen, Z.; Whittingham, M.S.; Strømman, A.H. Nanotechnology for environmentally sustainable electromobility. *Nat. Nanotechnol.* **2016**, *486*, 43–51. [[CrossRef](#)] [[PubMed](#)]
3. Wu, G.; More, K.L.; Johnston, C.M.; Zelenay, P. High-performance electrocatalysts for oxygen reduction derived from polyaniline, iron, and cobalt. *Science* **2011**, *332*, 443–447. [[CrossRef](#)] [[PubMed](#)]
4. Chen, Z.; Waje, M.; Li, W.; Yan, Y. Supportless Pt and PtPd nanotubes as electrocatalysts for oxygen-reduction reactions. *Angew. Chem. Int. Ed.* **2007**, *46*, 4060–4063. [[CrossRef](#)] [[PubMed](#)]
5. Gong, K.; Du, F.; Xia, Z.; Durstock, M.; Dai, L. Nitrogen-doped carbon nanotube arrays with high electrocatalytic activity for oxygen reduction. *Science* **2009**, *323*, 760–764. [[CrossRef](#)]
6. Dai, L.; Xue, Y.; Qu, L.; Choi, H.J.; Baek, J.B. Metal-free catalysts for oxygen reduction reaction. *Chem. Rev.* **2015**, *115*, 4823–4892. [[CrossRef](#)]

7. Bezerra, C.W.; Zhang, L.; Lee, K.; Liu, H.J.; Marques, A.L.; Marques, E.P.; Wang, H.; Zhang, J. A review of Fe–N/C and Co–N/C catalysts for the oxygen reduction reaction. *Electrochem. Acta* **2008**, *53*, 4937–4951. [[CrossRef](#)]
8. Nabae, Y.; Nagata, S.; Kusaba, K.; Aoki, T.; Hayakawa, T.; Tanida, H.; Imai, H.; Hori, K.; Yamamoto, Y.; Arai, S.; et al. Magnetic purification of non-precious metal fuel cell catalysts for obtaining atomically dispersed Fe centers. *Catal. Sci. Technol.* **2020**, *10*, 493–501. [[CrossRef](#)]
9. Nabae, Y.; Sonoda, M.; Yamauchi, C.; Hosaka, Y.; Isoda, A.; Aoki, T. Highly durable Pt-free fuel cell catalysts prepared by multi-step pyrolysis of Fe phthalocyanine and phenolic resin. *Catal. Sci. Technol.* **2014**, *4*, 1400–1406. [[CrossRef](#)]
10. Liu, W.; Zhang, L.; Yan, W.; Liu, X.; Yang, X.; Miao, S.; Wang, W.; Wang, A.; Zhang, T. Single-atom dispersed Co–N–C catalyst: Structure identification and performance for hydrogenative coupling of nitroarenes. *Chem. Sci.* **2016**, *7*, 5758–5764. [[CrossRef](#)]
11. Yin, P.; Yao, T.; Wu, Y.; Zheng, L.; Lin, Y.; Liu, W.; Ju, H.; Zhu, J.; Hong, X.; Deng, Z.; et al. Single cobalt atoms with precise N-coordination as superior oxygen reduction reaction catalysts. *Angew. Chem. Int. Ed.* **2016**, *128*, 10958–10963. [[CrossRef](#)]
12. Wu, G.; Santandreu, A.; Kellogg, W.; Gupta, S.; Ogoke, O.; Zhang, H.; Wang, H.L.; Dai, L. Carbon nanocomposite catalysts for oxygen reduction and evolution reactions: From nitrogen doping to transition-metal addition. *Nano Energy* **2016**, *29*, 83–110. [[CrossRef](#)]
13. Lefevre, M.; Proietti, E.; Jaouen, F.; Dodelet, J.P. Iron-based catalysts with improved oxygen reduction activity in polymer electrolyte fuel cells. *Science* **2009**, *324*, 71–74. [[CrossRef](#)]
14. Jasinski, R. A new fuel cell cathode catalyst. *Nature* **1964**, *201*, 1212–1213. [[CrossRef](#)]
15. Li, J.; Xue, M.; Xu, N.; Zhang, X.; Wang, Y.; He, R.; Huang, H.; Qiao, J. Co/Ni dual-metal embedded in heteroatom doped porous carbon core-shell bifunctional electrocatalyst for rechargeable Zn-air batteries. *Mater. Rep. Energy* **2022**, *2*, 100090. [[CrossRef](#)]
16. Xu, X.; Su, C.; Shao, Z. Fundamental Understanding and Application of Ba_{0.5}Sr_{0.5}Co_{0.8}Fe_{0.2}O_{3-δ} Perovskite in Energy Storage and Conversion: Past, Present, and Future. *Energy Fuels* **2021**, *35*, 13585–13609. [[CrossRef](#)]
17. Zhang, X.; Xu, X.; Yao, S.; Hao, C.; Pan, C.; Xiang, X.; Tian, Z.Q.; Shen, P.K.; Shao, Z.; Jiang, S.P. Boosting Electrocatalytic Activity of Single Atom Catalysts Supported on Nitrogen-Doped Carbon through N Coordination Environment Engineering. *Small* **2022**, *18*, 2105329. [[CrossRef](#)]
18. Zitolo, A.; Goellner, V.; Armel, V.; Sougrati, M.T.; Mineva, T.; Stievano, L.; Fonda, E.; Jaouen, F. Identification of catalytic sites for oxygen reduction in iron-and nitrogen-doped graphene materials. *Nat. Mater.* **2015**, *14*, 937–942. [[CrossRef](#)]
19. Sahraie, N.R.; Kramm, U.I.; Steinberg, J.; Zhang, Y.; Thomas, A.; Reier, T.; Paraknowitsch, J.-P.; Strasser, P. Quantifying the density and utilization of active sites in non-precious metal oxygen electroreduction catalysts. *Nat. Commun.* **2015**, *6*, 8618. [[CrossRef](#)]
20. Fei, H.; Dong, J.; Feng, Y.; Allen, C.S.; Wan, C.; Voloskiy, B.; Li, M.; Zhao, Z.; Wang, Y.; Sun, H.; et al. General synthesis and definitive structural identification of MN₄C₄ single-atom catalysts with tunable electrocatalytic activities. *Nat. Catal.* **2018**, *1*, 63–72. [[CrossRef](#)]
21. Malko, D.; Kucernak, A.; Lopes, T. In situ electrochemical quantification of active sites in Fe–N/C non-precious metal catalysts. *Nat. Commun* **2016**, *7*, 13285. [[CrossRef](#)] [[PubMed](#)]
22. Yang, L.; Cheng, D.; Xu, H.; Zeng, X.; Wan, X.; Shui, J.; Xiang, Z.; Cao, D. Unveiling the high-activity origin of single-atom iron catalysts for oxygen reduction reaction. *Proc. Natl. Acad. Sci. USA* **2018**, *115*, 6626–6631. [[CrossRef](#)] [[PubMed](#)]
23. Li, Y.; Liu, X.; Zheng, L.; Shang, J.; Wan, X.; Hu, R.; Guo, X.; Hong, S.; Shui, J. Preparation of Fe–N–C catalysts with FeN_x (x = 1, 3, 4) active sites and comparison of their activities for the oxygen reduction reaction and performances in proton exchange membrane fuel cells. *J. Mater. Chem.* **2019**, *7*, 26147–26153. [[CrossRef](#)]
24. Wen, Y.; Ma, C.; Wei, Z.; Zhu, X.; Li, Z. FeNC/MXene hybrid nanosheet as an efficient electrocatalyst for oxygen reduction reaction. *RSC Adv.* **2019**, *9*, 13424–13430. [[CrossRef](#)] [[PubMed](#)]
25. Zhang, Z.; Sun, J.; Wang, F.; Dai, L. Efficient oxygen reduction reaction (ORR) catalysts based on single iron atoms dispersed on a hierarchically structured porous carbon framework. *Angew. Chem. Int. Ed.* **2018**, *130*, 9176–9181. [[CrossRef](#)]
26. Lin, L.; Zhu, Q.; Xu, A.-W. Noble-metal-free Fe–N/C catalyst for highly efficient oxygen reduction reaction under both alkaline and acidic conditions. *J. Am. Chem. Soc.* **2014**, *136*, 11027–11033. [[CrossRef](#)]
27. Zhu, C.; Fu, S.; Song, J.; Shi, Q.; Su, D.; Engelhard, M.H.; Li, X.; Xiao, D.; Li, D.; Estevez, L.; et al. Self-Assembled Fe–N-Doped Carbon Nanotube Aerogels with Single-Atom Catalyst Feature as High-Efficiency Oxygen Reduction Electrocatalysts. *Small* **2017**, *13*, 16004–16007. [[CrossRef](#)]
28. Ao, X.; Zhang, W.; Li, Z.; Lv, L.; Ruan, Y.; Wu, H.H.; Chiang, W.H.; Wang, C.; Liu, M.; Zeng, X.C. Unraveling the high-activity nature of Fe–N–C electrocatalysts for the oxygen reduction reaction: The extraordinary synergy between Fe–N₄ and Fe₄–N. *J. Mater. Chem. A* **2019**, *7*, 11792–11801. [[CrossRef](#)]
29. Wang, X.; Fang, J.; Liu, X.; Zhang, X.; Lv, Q.; Xu, Z.; Zhang, X.; Zhu, W.; Zhuang, Z. Converting biomass into efficient oxygen reduction reaction catalysts for proton exchange membrane fuel cells. *Sci. China Mater.* **2020**, *63*, 524–532. [[CrossRef](#)]
30. Zhang, H.; Song, X.; Zhao, C.; Hu, D.; Zhang, W.; Jia, M. N-Doped Porous Carbon–Fe_xC Nanoparticle Composites as Catalysts for Friedel–Crafts Acylation. *ACS Appl.* **2020**, *3*, 6664–6674.
31. Xiao, M.; Zhu, J.; Ma, L.; Jin, Z.; Ge, J.; Deng, X.; Hou, Y.; He, Q.; Li, J.; Jia, Q.; et al. Microporous framework induced synthesis of single-atom dispersed Fe–NC acidic ORR catalyst and its in situ reduced Fe–N₄ active site identification revealed by X-ray absorption spectroscopy. *ACS Catal.* **2018**, *8*, 2824–2832. [[CrossRef](#)]

32. Qiao, Y.; Yuan, P.; Hu, Y.; Zhang, J.; Mu, S.; Zhou, J.; Li, H.; Xia, H.; He, J.; Xu, Q. Sulfuration of an Fe–N–C catalyst containing Fe_xC/Fe species to enhance the catalysis of oxygen reduction in acidic media and for use in flexible Zn–air batteries. *Adv. Mater.* **2018**, *30*, 1804504. [[CrossRef](#)]
33. Chen, Y.; Ji, S.; Wang, Y.; Dong, J.; Chen, W.; Li, Z.; Shen, R.; Zheng, L.; Zhuang, Z.; Wang, D.; et al. Isolated single iron atoms anchored on N-doped porous carbon as an efficient electrocatalyst for the oxygen reduction reaction. *Angew. Chem. Int. Ed.* **2017**, *129*, 7041–7045. [[CrossRef](#)]
34. Zhang, M.; Wang, Y.G.; Chen, W.; Dong, J.; Zheng, L.; Luo, J.; Wan, J.; Tian, S.; Cheong, W.C.; Wang, D.; et al. Metal (hydr) oxides@ polymer core–shell strategy to metal single-atom materials. *J. Am. Chem. Soc.* **2017**, *139*, 10976–10979. [[CrossRef](#)]
35. Shui, J.; Wang, M.; Du, F.; Dai, L. N-doped carbon nanomaterials are durable catalysts for oxygen reduction reaction in acidic fuel cells. *Sci. Adv.* **2015**, *1*, e1400129. [[CrossRef](#)]
36. Prieto, R.; Louis, E.; Molina, J. Fabrication of mesophase pitch-derived open-pore carbon foams by replication processing. *Carbon* **2012**, *50*, 1904–1912. [[CrossRef](#)]
37. Alway-Cooper, R.M.; Anderson, D.P.; Ogale, A.A. Carbon black modification of mesophase pitch-based carbon fibers. *Carbon* **2013**, *59*, 40–48. [[CrossRef](#)]
38. Li, M.; Liu, D.; Du, H.; Li, Q.; Hou, X.; Ye, J. Preparation of mesophase pitch by aromatics-rich distillate of naphthenic vacuum gas oil. *Appl. Petrochem. Res.* **2015**, *5*, 339–346. [[CrossRef](#)]
39. Liu, D.; Lou, B.; Li, M.; Qu, F.; Yu, R.; Yang, Y.; Wu, C. Study on the preparation of mesophase pitch from modified naphthenic vacuum residue by direct thermal treatment. *Energy Fuels* **2016**, *30*, 4609–4618. [[CrossRef](#)]
40. Guo, J.; Zhu, H.; Xu, H.; Westwood, A.; Li, X. Spinnable mesophase pitch prepared via co-carbonization of fluid catalytic cracking decant oil and synthetic naphthalene pitch. *Energy Fuels* **2019**, *34*, 2566–2573. [[CrossRef](#)]
41. Minato, H.; Higasaki, N.; Isobe, C. Polymerization of Naphthalene and Reactions of Polynaphthalene. *Bull. Chem. Soc. Jpn.* **1969**, *42*, 779–781. [[CrossRef](#)]
42. Korai, Y.; Mochida, I. Molecular assembly of mesophase and isotropic pitches at their fused states. *Carbon* **1992**, *30*, 1019–1024. [[CrossRef](#)]
43. Mushrush, G.W.; Beal, E.J.; Hardy, D.R.; Hughes, J.M. Nitrogen compound distribution in middle distillate fuels derived from petroleum, oil shale, and tar sand sources. *Fuel Process. Technol.* **1999**, *61*, 197–210. [[CrossRef](#)]
44. Xu, Z.; Zhou, Y.; Sun, Z.; Zhang, D.; Huang, Y.; Gu, S.; Chen, W. Understanding reactions and pore-forming mechanisms between waste cotton woven and FeCl₃ during the synthesis of magnetic activated carbon. *Chemosphere* **2020**, *241*, 125120. [[CrossRef](#)]
45. Abthagir, P.S.; Dhanalakshmi, K.; Saraswathi, R. Thermal studies on polyindole and polycarbazole. *Synth. Met.* **1998**, *93*, 1–7. [[CrossRef](#)]
46. Artyushkova, K.; Serov, A.; Rojas-Carbonell, S.; Atanassov, P. Chemistry of multitudinous active sites for oxygen reduction reaction in transition metal–nitrogen–carbon electrocatalysts. *J. Phys. Chem. C* **2015**, *119*, 25917–25928. [[CrossRef](#)]
47. Ramaswamy, N.; Tylus, U.; Jia, Q.; Mukerjee, S. Activity descriptor identification for oxygen reduction on nonprecious electrocatalysts: Linking surface science to coordination chemistry. *J. Am. Chem. Soc.* **2013**, *135*, 15443–15449. [[CrossRef](#)]
48. Jia, Q.; Ramaswamy, N.; Hafiz, H.; Tylus, U.; Strickland, K.; Wu, G.; Barbiellini, B.; Bansil, A.; Holby, E.F.; Zelenay, P.; et al. Experimental Observation of Redox-Induced Fe–N Switching Behavior as a Determinant Role for Oxygen Reduction Activity. *ACS Nano* **2015**, *9*, 12496–12505. [[CrossRef](#)]
49. Chung, H.T.; Cullen, D.A.; Higgins, D.; Sneed, B.T.; Holby, E.F.; More, K.L.; Zelenay, P. Direct atomic-level insight into the active sites of a high-performance PGM-free ORR catalyst. *Science* **2017**, *357*, 479–484. [[CrossRef](#)]